Final Report for Task 5 of USGS NGA-Ground Motion Support Project funded by the USNRC

Refinements to the Graves and Pitarka (2010) Broadband Ground Motion Simulation Method

Robert Graves

Introduction

This brief report describes refinements to the Graves and Pitarka (2010) broadband ground motion simulation methodology (GP2010 hereafter) that have been implemented in version 14.3 of the SCEC Broadband Platform (BBP). The updated version of our method on the current SCEC BBP is referred to as GP14.3. Our simulation technique is a hybrid approach that combines low-frequency and high-frequency motions computed with different methods into a single broadband response. The separate low- and high-frequency components have traditionally been called "deterministic" and "stochastic", respectively; however, this nomenclature is an oversimplification. In reality, the low-frequency approach includes many stochastic elements, and likewise, the high-frequency approach includes many deterministic elements (e.g., Pulido and Kubo, 2004; Hartzell et al., 2005; Liu et al., 2006; Frankel, 2009; Graves and Pitarka, 2010; Mai et al., 2010). While the traditional terminology will likely remain in use by the broader modeling community, in this paper we will refer to these using the generic terminology "low-frequency" and "high-frequency" approaches. Furthermore, one of the primary goals in refining our methodology is to provide a smoother and more consistent transition between the low- and high-frequency calculations, with the ultimate objective being the development of a single unified modeling approach that can be applied over a broad frequency band.

GP2010 was validated by modeling recorded strong motions from four California earthquakes. While the method performed well overall, several issues were identified including the tendency to over-predict the level of longer period (2-5 sec) motions and the

effects of rupture directivity. The refinements incorporated in GP14.3 are aimed at addressing these issues with application to the simulation of earthquakes in Western US (WUS). These refinements include the addition of a deep weak zone (details in following section) to the rupture characterization and allowing perturbations in the correlation of rise time and rupture speed with the specified slip distribution. Additionally, we have extended the parameterization of GP14.3 so that it is also applicable for simulating Eastern North America (ENA) earthquakes. This work has been guided by the comprehensive set of validation studies described in Goulet and Abrahamson (2014) and Dreger et al. (2014). The GP14.3 method shows improved performance relative to GP2010, and we direct the interested reader to Dreger et al. (2014) for a detailed assessment of the current methodology. In this paper, we concentrate on describing the modifications in more detail, and also discussing additional refinements that are currently being developed.

How Deep Do Crustal Earthquake Ruptures Go?

The down-dip coseismic rupture extent for large magnitude (M~7 and above) crustal earthquakes is a poorly resolved parameter. Inversions of past earthquakes utilizing both geodetic and strong motion data have decreasing resolution with increasing depth, and thus the data can be satisfied with models having quite a range of rupture widths (e.g., Delouis et al., 2002; Sekiguchi and Iwata, 2002). Traditionally, background seismicity and/or aftershock locations have been used to define the geometry and location of rupture (e.g. Wald et al., 1996); however, this can be problematic since large displacement ruptures may penetrate a significant distance into the more ductile region of the crust, which may (e.g., Rolandone et al., 2004;) or may not be illuminated by aftershocks (e.g., Scholz, 1998; Noda and Lapusta, 2013). The uncertainty of rupture width is a significant component of the scatter in estimated rupture areas of past earthquakes, and may also lead to apparent inconsistencies in the scaling of earthquake magnitude with fault area, particularly at larger magnitudes (e.g., Wells and Coppersmith, 1994; Hanks and Bakun, 2008; Leonard, 2010).

Our experience in modeling large magnitude earthquake ruptures is that defining the rupture width based on background seismicity (e.g., Hanks and Bakun, 2008) concentrates the fault slip in the shallow portion of the crust and leads to an over estimation of long period motions (Graves et al., 2010). Allowing the large magnitude ruptures to penetrate deeper into the crust while keeping the seismic moment fixed results in a reduction of longer period motions due to the corresponding decrease in average fault displacement. With the GP14.3 simulation approach, we have found the magnitude-length and magnitude-area scaling relations of Leonard (2010) provide the best fit for the earthquakes we have modeled, and in our opinion are the most consistent with the inferred depth

extent of coseismic displacement. The Leonard (2010) relations set the maximum rupture depth for strike-slip events in active tectonic regions at 19 km.

While rupture beneath the depth of background seismicity is likely to occur in large earthquakes, the distance it will travel into this ductile zone not certain. In our current parameterization for active tectonic environments, we transition into this zone over a generic depth range of 15 to 18 km by applying a linear adjustment in the scaling of rupture speed, rise time and corner frequency (details in following section).

Refinements for Western US (WUS) Applications

The refinements to our current methodology for WUS events involve a combination of relatively minor adjustments to key rupture parameters, as well as the addition of stochastic perturbations of these parameters about their median values. The goal is to reduce the coherence of radiated motions around 1 to 2 sec period and provide a smoother transition between the low- and high-frequency calculations.

Rise Time/Corner Frequency Scaling

As defined in GP2010, the subfault corner frequency (f_{ci}) and average slip rise time (τ_A) are given by the following relations,

$$f_{ci} = \frac{c_0 \, V_{Ri}}{\alpha_T \, \pi \, dl} \tag{1}$$

$$\tau_A = \alpha_T \, c_1 \, M_o^{1/3} \tag{2}$$

where V_{Ri} is the local rupture speed, dl is the average subfault dimension, M_o is the seismic moment, α_T is a mechanism-dependent scaling factor (defined below), and c_0 and c_1 are constants. In GP2010, c_0=2.1 and c_1=1.6 x 10^{-9}. Based on the results of the validation tests used in the development of GP14.3, these have been changed to c_0=2.0 and c_1=1.45 x 10^{-9}.

Additionally, in GP14.3 the scaling factor α_T is now a continuous function of fault rake (λ) and dip (δ), and is given by

$$\alpha_T = [1 + F_D \, F_R \, c_\alpha]^{-1} \tag{3}$$

with

$$F_D = \begin{cases} 1 - {(\delta - 45°)}/{45°}, & 45° < \delta \leq 90° \\ 1, & \delta \leq 45° \end{cases} \quad (4)$$

$$F_R = \begin{cases} 1 - {|\lambda - 90°|}/{90°}, & 0 \leq \lambda \leq 180° \\ 0, & \text{otherwise} \end{cases} \quad (5)$$

and c_α=0.1. As described in GP2010, this factor acts to increase the high frequency radiation for reverse faults.

Perturbations to Rupture Initiation Timing and Local Rise Time

GP2010 employed a scaling of the rupture speed with the local slip such that the rupture speed increases with increasing slip. In GP14.3, we retain this same basic scaling; however, we also add a random perturbation to this value so the rupture speed is no longer correlated 1:1 with the local slip. This is implemented by first determining the change in initiation time (Δt_0) given by the change in rupture speed assuming it is correlated 1:1 with local slip (i.e., equations 5 and 6 of GP2010). This value is then randomly perturbed using the following relation,

$$\Delta t = \Delta t_0 \exp(\varepsilon \sigma_T) \quad (6)$$

where ε is a random number selected from a standard normal distribution (mean of zero, standard deviation of one) and σ_T is the log-normal standard deviation, which is set to 0.2 in GP14.3 based on the validations described in Dreger et al. (2014).

GP2010 also scaled the subfault rise time with the square root of local slip such that the rise time averaged across the entire fault matched the empirical relation of Somerville et al. (1999). Additionally, the rise time was doubled in the shallow part of the fault (above 5 km depth) to represent the weakening of fault properties in the near surface. In GP14.3, we retain this same basic scaling, and we also impose another weak zone along the deeper portion of the fault characterized by a factor of two linear increase in rise time occurring over a depth of 3 km starting at 15 km or the hypocentral depth, whichever is greater. The choice of 15 km is taken as a representative thickness of the brittle crust in active regions (e.g., Hanks and Bakun, 2008; Shaw, 2013). These shallow and deep weak zones represent the transition from unstable to stable slip both in the near surface and as the fault reaches more ductile material in the midcrust (e.g., Scholz, 1998).

In addition, GP14.3 also adds a random perturbation to the subfault rise time so it is no longer correlated 1:1 with the square root of local slip. This is implemented by first

determining the subfault rise time (τ_{0i}) assuming a 1:1 correlation with the square root of slip (i.e., equation 7 of GP2010). This value is then randomly perturbed using the following relation,

$$\tau_i = \tau_{0i} \exp(\varepsilon \sigma_R) \quad (7)$$

where ε is a random number selected from a standard normal distribution and σ_R is the log-normal standard deviation, which is set to 0.5 in GP14.3 based on the validations described in Dreger et al. (2014).

Including the above perturbations significantly increases the short length scale complexity of both the rise time distribution and propagation of the rupture front in GP14.3 compared to GP2010. This is illustrated in Figure 1, which compares scenario rupture models for the Loma Prieta earthquake generated with different versions of our methodology. The perturbations resulting from the application of equations (7) and (8) are essentially stochastic representations of the short length scale distortions in the rupture that have been observed in dynamic rupture simulations incorporating geometric complexities in the fault surface or strongly heterogeneous initial stress conditions (e.g., Andrews and Barall, 2011; Dunham et al., 2011). While our simple perturbation approach produces variations that are uncorrelated from subfault to subfault, the longer length scale features of rise time and rupture time still retain the general correlation with the underlying slip distribution. Developing a more sophisticated correlation structure for these parameters is certainly possible and is the subject of ongoing research.

Using the rupture models in Figure 1, we have simulated motions for the Loma Prieta earthquake and compared with the observed motions. Figure 2 displays the spectral acceleration goodness-of-fit (GOF) for these simulations using the format described in Goulet and Abrahamson (2014). In order to concentrate on the source effects, we have limited this comparison to the 29 sites within 50 km closest distance to the rupture. For this scenario, the GP2010 result shows an over-prediction of about 10-20% for periods between 0.2 and 1 second, which increases to about 40-50% for periods between 2 and 5 seconds. The GP14.3 result still has a slight over-prediction, but shows a significantly improved fit across all periods.

Further Refinements under Development

We are currently exploring additional refinements to the rupture characterization. These include allowing large-scale variations in the background rupture speed, increasing the rise time up to a factor of four and applying a 30% reduction in the rupture speed in the deep weak zone, and adding stochastic perturbations to the subfault corner frequency in a

manner similar to that done for rise time. The far right column of Figure 1 shows a scenario rupture resulting from the inclusion of these modifications to the GP14.3 model (labeled v3.3.2). The primary visible differences are the slowing of the rupture and lengthening of the rise time along the bottom portion of the fault. The GOF resulting from this scenario is shown in the far right column of Figure 2. These additional modifications provide a further reduction in the strength of the 2 to 5 second period energy, as well as a reduction in the coherence of radiated motions around 1 second period, resulting in a smoother transition between the low- and high-frequency responses.

Application to Eastern North America (ENA)

Thus far, we have modeled three ENA earthquakes: M4.7 Riviere du Loup, M5.7 Mineral, and M5.9 Saguenay. Detailed descriptions of the source geometries, velocity models and station sets used for these simulations are provided in Goulet and Abrahamson (2014) and Dreger et al. (2014).

Basic ENA Parameterization

For the initial application to ENA events, the following modifications were made to the simulation methodology:

- Increasing the average rise time by 86% and decreasing the average corner frequency by 46%, relative to WUS values (following Somerville et al., 2009).
- Setting the high-frequency stress parameter to 150 bars (following Somerville et al., 2009).
- Using the Leonard (2010) SCR magnitude-length and magnitude-area scaling relations.
- Setting the high-frequency Q parameters in equations (14) and (15) of GP2010 to a=228, b=136 and x=0.45, and setting κ=0.01 in equation (16) of GP2010 (following Beresnev and Atkinson, 2002).
- Setting the background rupture speed to 85% of local shear wave velocity (WUS uses 80% of local shear wave velocity).
- Removing the shallow and deep weak zones from the rupture characterization.

The increase in background rupture speed relative to WUS was found to provide a marginally better fit to the events analyzed. The removal of the shallow and deep weak zone from the parameterization was prompted by a lack of evidence supporting these features given the limited amount of ENA data.

As shown in Dreger et al. (2014), the above parameterization works well for Riviere du Loup, slightly under-predicts the longer periods for Mineral, and significantly under-predicts all periods for Saguenay. For Mineral, we have found that simply moving the top of the fault from 5.8 km to 3 km depth noticeably improves the longer period fit (Figure 3). We suspect that this may result in more efficient trapping of surface waves that contribute to the longer period response.

Refined ENA Parameterization

Using a trial-and-error approach, we found an improved fit for Saguenay can be obtained by applying the following modifications to the basic ENA parameters:

- Increasing the stress parameter by a factor of 3 (to 450 bars).
- Scaling the fault rupture area by a factor of $3^{-2/3}$ (following area $\sim \Delta\sigma^{-2/3}$).
- Increasing the background rupture speed to 95% of local shear wave velocity.
- Reducing the coefficient of variation in slip variability to 0.4, which produces a smoother slip distribution (standard COV value is 0.85).

Figure 4 compares the GOF results for Saguenay using the basic (top panel) and refined (bottom panel) ENA parameterizations. The results shown in Figure 4 are averaged over 50 realizations. Clearly, the refined approach provides a much better fit to the average level of the ground motions relative to that obtained with the basic parameter set.

Since Saguenay is a much deeper event (~ 28 km) compared to the other ENA events we have considered, it suggests a depth scaling of the rupture parameterization may be warranted. Furthermore, the recent work by Boatwright and MacDonald (2012) suggests that events in eastern Quebec (including Saguenay) show stress drop increasing with increasing depth. Guided by this, our current recommendation for general application to ENA events is to apply a linear scaling from the basic parameters at 10 km depth to the above parameters at 25 km depth.

The Saguenay Quandary

The 1988 M5.9 Saguenay earthquake has long been a source of uncertainty in understanding ENA seismic hazards. In general, the ground motions for this event are quite large over a fairly broad frequency range and various mechanisms have been put forth over the years to explain the cause of these motions (e.g., Somerville et al, 1990; Boore and Atkinson, 1992; Hartzell et al., 1994; Haddon, 1995). These include high stress drop, radiation pattern, rupture directivity, wave propagation effects, geometric spreading

and Q. Our approach outlined in the preceding section primarily relies on an increased static stress drop to model this event.

However, we also recognize that high static stress drop alone cannot match all of the features of the Saguenay records. Figure 5 plots recorded 1-second spectral acceleration as a function of distance for the Saguenay earthquake along with values simulated using our model and the prediction from the GMPE of Atkinson and Boore (2011). All responses are corrected to V_{s30} = 1000 m/s. The two nearest recording sites are north of the epicenter and show anomalously low amplitudes, while the sites around 100 km distance are to the south along the St. Lawrence Seaway (magenta symbols) and show amplitudes that are 5-6 times larger than the closer sites. While the simulations capture the average trend of the recorded motions, they cannot replicate the large amplification in the St. Lawrence region or the low amplitude response of the closer stations. This suggests that other factors such as site response or lateral velocity variations in the deep or mid-crust may also play a role. Incorporation of these effects is beyond the scope of the present set of calculations; however, a more thorough investigation of the significance of these factors is certainly warranted.

Conclusions

In this paper, we describe refinements to the GP2010 simulation method that have been guided by studies using the SCEC BBP (Goulet and Abrahamson, 2014; Dreger et al., 2014), leading to the development of version GP14.3. One refinement involves the addition of a deep weak zone to the rupture characterization, analogous to the shallow weak zone introduced by GP2010. This modification reduces the radiation of strong motion energy from the deep fault while still allowing large fault displacement to occur in this zone. The result is to reduce the tendency of the simulations to over-predict observed ground motion levels in the period range of 2 to 5 sec, particularly for larger magnitude ruptures. A second refinement adds stochastic perturbations to the correlation structure for rise time and rupture speed parameterization. The effect is to reduce the coherence of radiated motions around 1 to 2 sec period and provide a smoother transition between the low- and high-frequency calculations. GP14.3 also extends our methodology to be applicable for simulation of ENA earthquakes. This requires an increase in stress parameter, static stress drop, average rupture speed and rise time relative to WUS values, removal of the shallow and deep weak zones from the rupture characterization, as well as adjustment of Q and kappa. In order to match the average levels of the 1988 M5.9 Saguenay earthquake, we must further increase the stress parameter by a factor of 3, accompanied by a reduction in fault area of $3^{-2/3}$. For general ENA applications, we propose a depth-dependent linear increase of stress parameter, static stress drop and rupture speed over the depth range from 10 to 25 km that is consistent with our modeling of the 3 ENA earthquakes. We

recognize that this parameterization is controlled by the Saguenay event, and thus may need modification as additional ENA data become available. Overall, GP14.3 offers improved performance compared to GP2010, and it has successfully passed the evaluation and validation criteria set forth in Goulet and Abrahamson (2014) and Dreger et al. (2014).

References

Atkinson, G. M., and D. M. Boore (2011). Modifications to Existing Ground-Motion Prediction Equations in Light of New Data, *Bull. Seism. Soc. Am.*, **101**, 1121–1135, doi: 10.1785/0120100270.

Beresnev, I. A., and G. M. Atkinson (2002). Source Parameters of Earthquakes in Eastern and Western North America Based on Finite-Fault Modeling, *Bull. Seism. Soc. Am*., **92**, 695–710.

Boatwright, J., and T., MacDonald, (2012). The Variation of Brune Stress Drop with Hypocentral Depth for Moderate (2.5 ≤ M ≤ 5.8) Earthquakes in Northeastern North America, *Abstract presented at the Annual Meeting of the Eastern Section of SSA*, Blacksburg, VA, Oct. 28-30.

Boore, D. M., and G. M. Atkinson (1992). Source spectra for the 1988 Saguenay earthquakes, *Bull. Seism. Soc. Am*., **82**, 683-719.

Delouis, B., D. Giardini, P. Lundgren, and J. Salichon (2002). Joint inversion of InSAR, GPS, teleseismic, and strong-motion data for the spatial and temporal distribution of earthquake slip: Application to the 1999 Izmit mainshock, *Bull. Seism. Soc. Am*., **92**, 278-299.

Dreger, D., G. Beroza, S. Day, C. Goulet, P. Spudich, J. Stewart, and T. Jordan (2014). Evaluation of SCEC Broadband Platform Phase 1 PSA Ground Motion Simulation Results, *submitted to SRL*.

Dunham, E. M., D. Belanger, L. Cong, and J. E. Kozdon (2011). Earthquake Ruptures with Strongly Rate-Weakening Friction and Off-Fault Plasticity, Part 2: Nonplanar Faults, *Bull. Seism. Soc. Am*., **101**, 2308-2322, doi: 10.1785/0120100076.

Frankel, A. (2009). A constant stress-drop model for producing broadband synthetic seismograms: Comparison with the Next Generation Attenuation relations, Bull. Seismol. Soc. Am. 99, 664–680.

Goulet, C. A., and N. A. Abrahamson (2014). The SCEC Broadband Platform validation exercise for pseudo-spectral acceleration: methodology for code validation in the context of seismic hazard analyses, *submitted to SRL.*

Graves, R., S. Callaghan, E. Deelman, E. Field, T. H. Jordan, G. Juve, C. Kesselman, P. Maechling, G. Mehta, K. Milner, D. Okaya, P. Small, K. Vahi (2010). CyberShake: Full Waveform Physics-Based Probabilistic Seismic Hazard Calculations for Southern California, *PAGEOPH,* DOI 10.1007/s00024-010-0161-6.

Graves, R. W., and Arben Pitarka (2010). Broadband Ground-Motion Simulation Using a Hybrid Approach, *Bull. Seism. Soc. Am*., **100**, 2095–2123, doi: 10.1785/0120100057.

Haddon, R. A. W. (1995). Modeling of Source Rupture Characteristics for the Saguenay Earthquake of November 1988, *Bull. Seism. Soc. Am*., **85**, 525-551.

Hanks, T. C., and W. H. Bakun (2008). M-log A observations of recent large earthquakes, *Bull. Seism. Soc. Am*., **98**, 490-494.

Hartzell, S., C. Langer and C. Mendoza (1994). Rupture Histories of Eastern North American Earthquakes, *Bull. Seism. Soc. Am*., **84**, 1703-1724.

Hartzell, S., M. Guatteri, P. M. Mai, P. C. Liu, and M. Fisk (2005). Calculation of broadband time histories of ground motion, Part ii: Kinematic and dynamic modeling using theoretical green's functions and comparison with the 1994 Northridge earthquake, Bull. Seismol. Soc. Am. 95, 614–645.

Leonard, M. (2010). Earthquake fault scaling: Self-consistent relating of rupture length, width, average displacement, and moment release, *Bull. Seism. Soc. Am*. **100**, 1971-1988, doi: 10.1785/0120090189.

Liu, P., R. Archuleta, and S. Hartzell (2006). Prediction of broadband ground-motion time histories: Hybrid low/high-frequency method with correlated random source parameters, Bull. Seismol. Soc. Am. 96, 2118–2130.

Mai, P. M., W. Imperatori, and K. B. Olsen (2010). Hybrid broadband ground-motion simulations: Combining long-period deterministic synthetics with high-frequency multiple S-to-S backscattering, Bull. Seismol. Soc. Am. 101, 2124–2142.

Noda, H., and N. Lapusta (2013). Stable creeping fault segments can become destructive as a result of dynamic weakening, *Nature*, **493**, 518–521, doi:10.1038/nature11703.

Pulido, N., and T. Kubo (2004). Near-fault strong motion complexity of the 2000 Tottori earthquake (Japan) from a broadband source asperity model, Tectonophysics 390, 177–192.

Rolandone, F., R. Bürgmann, and R. M. Nadeau (2004). The evolution of the seismic–aseismic transition during the earthquake cycle: Constraints from the time-dependent depth distribution of aftershocks, *Geophys. Res. Lett*., **31**, L23610, doi: 10.1029/2004GL021379.

Scholz, C. H. (1998). Earthquakes and friction laws, *Nature*, **391**, 37-42.

Sekiguchi, H., and T. Iwata (2002). Rupture process of the 1999 Kocaeli, Turkey, earthquake estimated from strong-motion waveforms, *Bull. Seism. Soc. Am*., **92**, 300-311.

Shaw, B. E. (2013). Earthquake Surface Slip-Length Data is Fit by Constant Stress Drop and is Useful for Seismic Hazard Analysis, *Bull. Seism. Soc. Am*., **103**, 876–893, doi: 10.1785/0120110258.

Somerville, P. G., J. McLaren, C. Saikia, and D. Helmberger (1990). The Nov. 25, 1988 Saguenay, Quebec earthquake: source parameters and the attenuation of strong ground motion, *Bull. Seism. Soc. Am*., **80**, 1118-1143.

Somerville, P., K. Irikura, R. Graves, S. Sawada, D. J.Wald, N. Abrahmason, Y. Iwasaki, T. Kagawa, N. Smith, and A. Kowada (1999). Characterizing crustal earthquake slip models for the prediction of strong ground motion, *Seism. Res. Lett*., **70(1)**, 59–80.

Somerville, P., R. Graves, N. Collins, S.G. Song, S. Ni, and P. Cummins (2009). Source and Ground Motion Models for Australian Earthquakes, *Proc. 2009 Annual Conference of the Australian Earthquake Engineering Society*, Newcastle, Dec. 11-13.

Wald, D. J., T. H. Heaton, and K. W. Hudnut (1996). The slip history of the 1994 Northridge, California, earthquake determined from strong-motion, teleseismic, GPS, and leveling data, *Bull. Seism. Soc. Am*., **86**, S49–S70.

Wells, D. L., and K. J. Coppersmith (1994). New empirical relationships among magnitude, rupture length, rupture width, rupture area, and surface displacement, *Bull. Seism. Soc. Am*., **84**, 974-1002.

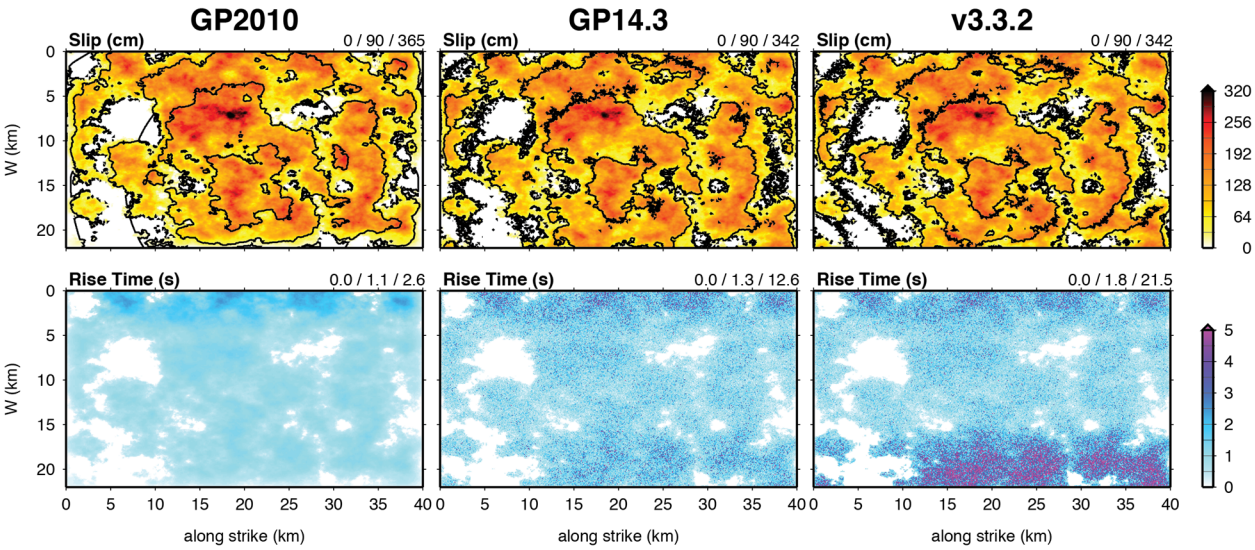

Figure 1. Kinematic rupture models generated with GP2010 (left), GP14.3 (center) and the development version v3.3.2 (right) of the simulation methodology for a scenario realization based on the 1989 Loma Prieta earthquake. Top row shows slip distribution (color scale) and rupture contours at 2 sec intervals. Bottom row shows rise time distribution. Aside from edge tapering in GP2010, the slip distribution is the same for all cases.

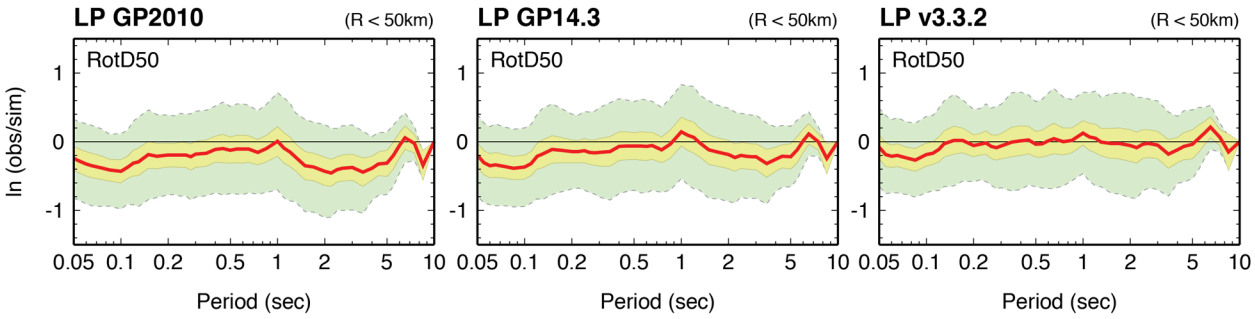

Figure 2. Spectral acceleration GOF for Loma Prieta simulations using the rupture models in Figure 1 for GP2010 (left), GP14.3 (center) and the development version v3.3.2 (right). Results are for 29 sites within 50 km of the rupture.

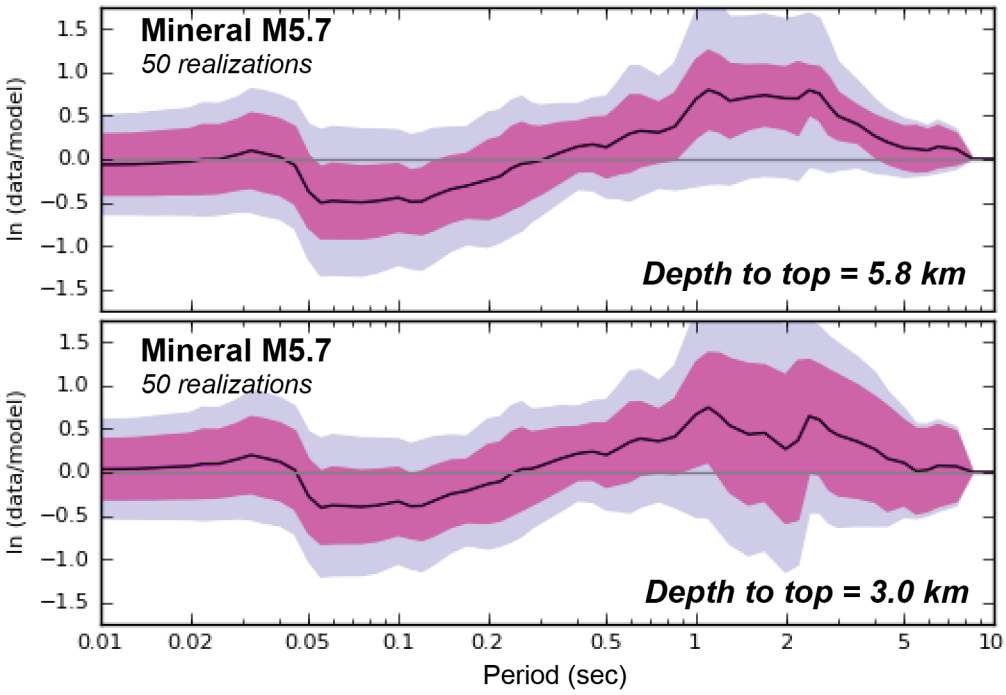

Figure 3. Spectral acceleration GOF for Mineral, VA simulations using GP14.3 averaged over 50 random realizations. Top panel shows results obtained using a fault depth of 5.8 km; bottom panel shows results obtained using a fault depth of 3 km.

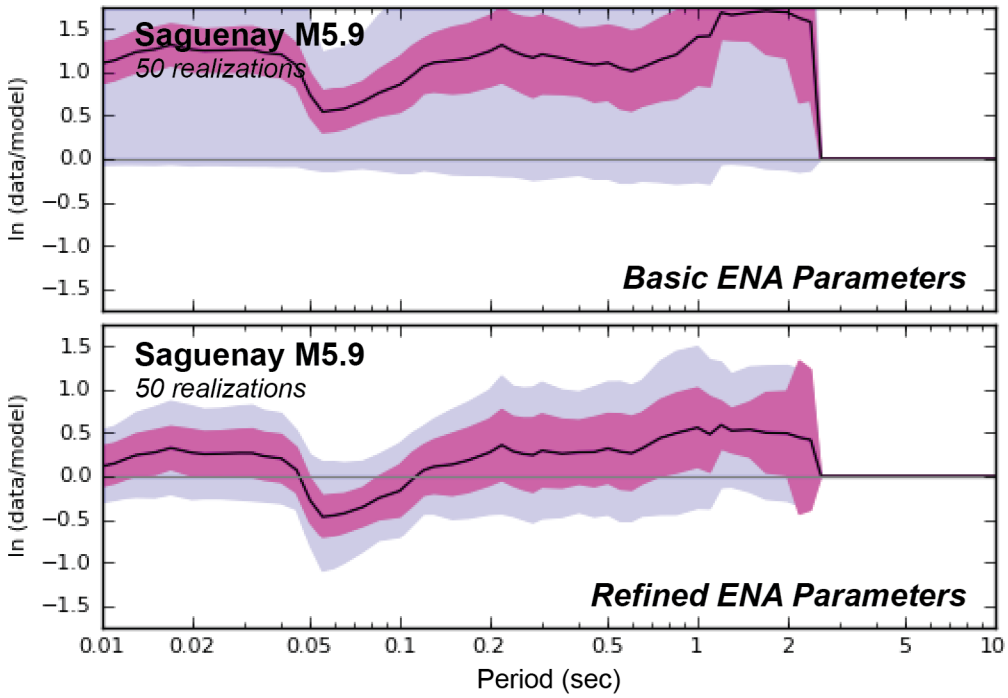

Figure 4. Spectral acceleration GOF for Saguenay simulations using GP14.3 averaged over 50 random realizations. Top panel shows results obtained using the basic ENA parameterization; bottom panel shows results obtained using the refined ENA parameterization.

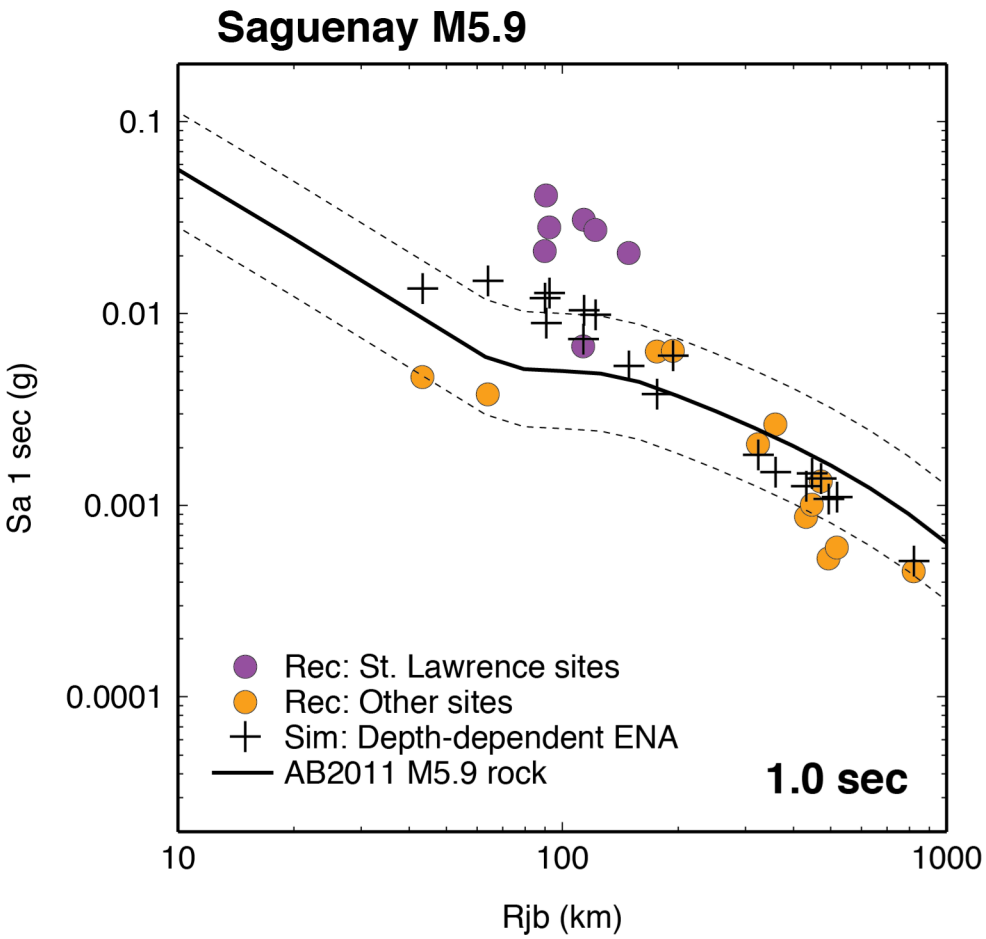

Figure 5. Observed (filled circles) and simulated (crosses) spectral acceleration at 1 second period plotted as a function of Joyner-Boore distance for the Saguenay earthquake. All responses are adjusted to V_{s30} = 1000 m/s. Solid and dashed lines are, respectively, the median and one standard deviation predictions for a rock site condition from the GMPE of Atkinson and Boore (2011). Magenta symbols indicate observed motions at sites along the St. Lawrence Seaway.

Ground-Motion Predictions for Eastern North American Earthquakes Using Hybrid Broadband Seismograms from Finite-Fault Simulations with Constant Stress-Drop Scaling

Arthur D. Frankel
U.S. Geological Survey

ABSTRACT

Broadband seismograms for M4.5, 5.5, 6.5, 7.5, and 8.0 eastern North American (ENA) earthquakes were calculated from physically-plausible, finite-fault simulations for rupture distances of 2-1000 km. PSA values were calculated from these synthetics, binned with respect to distance, and provided to the NGA-East TI team. The broadband synthetics were derived from combining deterministic synthetics for a plane-layered velocity model at low frequencies with stochastic synthetics at high frequencies, using matched filters. This follows the procedure described in Frankel (2009), which has been validated for several earthquakes and against NGA-West 1. The procedure uses a dynamic stress drop that is constant with magnitude for the low-frequency synthetics and a Brune stress drop that is constant with magnitude for the high-frequency synthetics. The stochastic synthetics assume a geometrical spreading of 1/R from 0-70 km distance. The 1 Hz PSA values controlled by the deterministic synthetics decay more steeply than predicted from a 1/R model, consistent with observations of Charlevoix earthquakes. The PSA values at higher frequencies exhibit saturation with magnitude at distances less than the rupture length. At larger distances, the PSA values at high frequencies are similar to the point source results of Frankel et al. (1996).

6.1 METHODOLOGY

The purpose of this study is to provide PSA values for ENA earthquakes derived from broadband seismograms determined from physically-plausible source models and propagation parameters. The hybrid procedure used in this study was described in detail in Frankel (2009) and combines low-frequency, finite-fault, deterministic synthetics for a plane-layered crustal model with high-frequency, finite-fault, stochastic synthetics that are based on summing stochastic point-source synthetics from SMSIM (Boore, 2005). The deterministic and stochastic synthetics are combined using matched filters to produce broadband synthetic seismograms (see Hartzell et al. 1999). Propagation and source parameters applied in the simulations were modified for ENA earthquakes from the Western U.S. (WUS) parameters used in Frankel (2009). The PSA values in this ENA study are for hard-rock sites with a Vs30 of 2.8 km/s. Note that the methodology has some similarities to that of Graves and Pitarka (2004), but with significant differences in how the source is specified and propagation parameters. I use the terms PSA and SA interchangeably in the text and figures of this chapter. All PSA and SA values are the pseudo-spectral accelerations. The values are the geometrical mean of the PSA values of the two horizontal components.

Frankel (2009) demonstrated that the WUS synthetics derived from this method produced PSA values similar to those predicted by NGA-West 1 for M5.5, 6.5, and 7.5 earthquakes, over distances of 5-200 km. The methodology was also validated using the strong-motion recordings of the Northridge, Loma Prieta, and Izmit earthquakes (Hartzell et al., 2011). Frankel (in press) showed that 1 Hz Fourier spectral amplitudes at distances of 10-80 km for the Riviere du Loup, Quebec earthquake were matched by the deterministic synthetics used in this procedure.

A key feature of the source model is constant stress drop scaling with moment. For the low-frequency deterministic synthetics, this is manifested by a constant dynamic stress drop for all magnitudes based on an average slip velocity of 5.4 m/s, twice that used for WUS earthquakes in Frankel (2009), in keeping with observations of intensities and stress drops of ENA earthquakes. Note that dynamic stress drop is proportional to slip velocity divided by rupture velocity. The average rupture velocity was also kept constant with magnitude. The average slip velocity and rupture velocity were not varied with depth. The high-frequency stochastic synthetics are derived from a summation of point-source synthetics each of which is calculated from a Brune (1970) stress drop of 200 bars, twice the value used for the WUS in Frankel (2009).

The low-frequency deterministic synthetics contain directivity effects from a propagating rupture, including forward directivity pulses, and also have the proper time delays for Moho reflections and surface waves. Low-frequency stochastic seismograms do not include the phasing of these essential features observed in actual seismograms. I used the southeastern Canada velocity and Q model of Hartzell et al. (1994) to construct the low-frequency synthetics (Table 1). The Q is independent of frequency. The synthetics were generated using the frequency-wavenumber integration code of Zhu and Rivera (2002). I developed random slip distributions with a wavenumber spectral falloff of k^{-2}, where k is

the wavenumber. The correlation distance of slip for each magnitude was scaled from the values specified in Mai and Beroza (2002), adjusting for twice the static stress drop (i.e., divided by the cube root of 2), such that the ratio of the correlation distance to overall rupture dimension was equal to that used for the WUS. A rupture cell (sub-event) size of 250m was used for all magnitudes. An average rupture velocity (v_{rave}) of 2.8 km/s was applied for all magnitudes. The secant rupture velocity at a given point on the fault plane was taken to be dependent on the final slip at that point, consistent with the results of dynamic simulations that showed higher rupture velocity in areas with high slip (see Frankel, 2009, 2013). The initiation time of rupture of each cell (sub-event) i is specified by

$$t_i = x_i / v_{ri} + \sigma_i + \varepsilon_j \qquad (1)$$

where x_i is the distance between the cell and the hypocenter. v_{ri} is the secant rupture velocity for that cell, which is dependent on the difference between the slip of that cell u_i and the average slip u_{ave} such that

$$v_{ri} = v_{rave} + c(u_i - u_{ave}) . \qquad (2)$$

Here c is a constant determined by specifying a 20% standard deviation of v_r. The rupture velocity perturbation of each cell is capped at ±0.4 v_{rave}. In equation (1) σ_i is a random value chosen from a uniform distribution from ±0.2 s. ε_j is a random value selected from a uniform distribution from ±0.4 s, applied to each square j with 5 cells on a side. This produces a small rupture velocity perturbation common within groups of neighboring cells.

The rise time of slip for each cell equals the final slip for that cell divided by the slip velocity at that point. A Brune (1970) pulse was used for each sub-event. Deterministic simulations were done for vertical strike slip faults and 45 degree dipping thrust faults (Table 2). For the latter, runs were done for rupture towards and away from the receivers.

For the high-frequency stochastic synthetics, I used a geometrical spreading of R^{-1} out to 70 km, R^0 from 70-130 km, and $R^{-0.5}$ for distances greater than 130 km, based on Atkinson and Boore (1995). Applying the R^{-1} geometrical spreading was motivated by recent analysis of a set of Charlevoix, Quebec earthquakes, in which I found that the apparent geometrical spreading steeper than R^{-1} observed at 1 Hz (Fourier spectral amplitude) at distances of less than 80 km could be explained by radiation pattern and directivity effects (Frankel, in press). The high frequency (14 Hz) observations for the Charlevoix earthquakes were consistent with a true geometrical spreading of R^{-1}. A Q= 680 $f^{0.36}$ was applied in the stochastic synthetics, based on Atkinson and Boore (1995) and consistent with their geometrical spreading parameters. I used a Vs30 of 2.8 km/s and a kappa of 0.006. The hard-rock shear-wave velocity profile used in the stochastic simulations was described in Frankel et al. (1996). The point-source stochastic synthetics were multiplied by a factor corresponding to a random distribution of stress drop over the rupture based on a k^{-1} fall-off of the wavenumber spectrum, using the same correlation distances and random number seed as the slip models (see Frankel, 2009). The moment of the sub-events was determined from the specified sub-event area assuming self-similar scaling such that area is proportional to (moment)$^{2/3}$. The sub-event areas fill the rupture

area of the earthquake being simulated, which results in a scaling of high-frequency Fourier spectral amplitude with moment consistent with an ω^{-2} high-frequency displacement spectral falloff (Frankel, 1995; 2009). Before combining with the low-frequency synthetics, the stochastic synthetic is convolved with a relative slip velocity function to ensure that its Fourier acceleration spectrum is flat with respect to frequency, for frequencies less than the corner frequency of the sub-event (see Frankel, 1995).

The crossover frequency between the deterministic and stochastic synthetics varied with magnitude (see Frankel, 2009), to reflect the differences in rise time and sub-event size, although caps in this frequency were applied for the largest and smaller magnitudes studied. For the M8.0 and M7.5 simulations, the crossover frequency was set to 0.8 Hz. For the M6.5 simulations, the crossover frequency was 2.4 Hz. For the M5.5 and M4.5 runs, the crossover frequency was 3.0 Hz.

For the M4.5, 5.5, 6.5, and the "thin-fault" runs for M7.5, the fault dimensions are reduced from the WUS values used in Frankel (2009), assuming that the ENA static stress drop is twice that for WUS, based on intensity data and stress-drop determinations (see fault dimension in Table 2). The fault dimensions for M4.5, 5.5, and 6.5 WUS earthquakes were derived from the M6.5 faulting dimensions found from empirical data by Wells and Coppersmith (1994) and using area proportional to $(\text{moment})^{2/3}$ (Frankel, 2009). Two geometries were used for the M7.5 ruptures ("thin" and "thick" faults), reflecting a range of aspect ratios, maximum depth, and area of faulting. The thin-fault runs use a length of 119 km and width of 12 km, based on scaling the WUS values in Frankel (2009). The WUS fault length for M7.5 was determined in Frankel (2009) from averaging the results of several empirical relations. For the "thick fault" ENA M7.5 runs, I used a fault length of 80 km and fault width of 25 km from Leonard (2010; SCR equations). The fault dimensions for the M8.0 runs were also taken from the Leonard (2010) SCR equations.

For most of the runs, the depth to top of rupture (Dtor) was 5 km (see Table 2). The M8.0 and M7.5 runs were for Dtor values of 1 and 5 km. There is one run with Dtor of 9 km for M5.5 and one run with Dtor of 12 km for M4.5 (Table 2). I have supplied the SA values from the Dtor= 1 km and Dtor ≥ 5 km runs in separate directories. Each SA value shown is the geometrical average of the SA values from the two horizontal components.

6.2 RESULTS

Synthetics were calculated for an array of sites at various distances and azimuths from the rupture, following Frankel (2009). The distance metric used is nearest distance to the rupture. The PSA values were provided to the NGA-East project as median values in distance bins.

Figure 6.2 shows the 5 Hz SA values from a sub-set of the simulations for M4.5, 5.5, 6.5, and 7.5. The results are compared with predictions (hard-rock sites) from Frankel et al. (1996) and Atkinson and Boore (2006; using different stress drops). At large distances

relative to the rupture dimension, the values from the finite-fault simulations are very close to those predicted from the point-source model of Frankel et al. (1996). This is expected since the propagation and stress drops for the high-frequency stochastic calculations were the same for the two models. At distances less than the rupture dimension, the SA values from the simulations level off with decreasing distance. At any given distance, the new simulations generally predict higher 5 Hz SA values than the models of Atkinson and Boore (2006), because I used a less steep geometrical spreading of 1/R in the first 70 km.

The 1 Hz SA values from the simulations are largely controlled by the deterministic calculations, with the exception of the M7.5 and M8.0 results, where the crossover frequency is 0.8 Hz and both portions of the hybrid synthetics are important. Figure 6.3 shows that the 1 Hz SA values from the simulations are less than those of Frankel et al. (1996) because they decay more steeply with distance in the first 70 km. This is caused by the effects of radiation pattern, directivity, and propagation through the flat-layered velocity model. The steep decay at 1 Hz is consistent with observations from the Charlevoix earthquakes studied by Frankel (in press). The 1 Hz SA values from the simulations are still a bit higher, at any given distance, than those predicted by Atkinson and Boore (2006).

Figures 6.4-6.7 compare the SA values from the simulations with the values from recordings of ENA earthquakes, as provided in the NGA East database. Here, I only plot the observed values for sites with Vs30 ≥ 760 m/s. I have not adjusted these values to Vs30 of 2800 m/s. For the M4.5 example, I used observed SA values from M4.0 to 5.0. For M5.5, I compared the predicted results with observed data from M5.0-5.8. I did not include observed SA values from the M5.8 Prague, OK earthquake. The point of these plots is to show that the data are generally consistent with the predicted values for M4.5 and M5.5 earthquakes out to 1000 km, at least for 1 Hz and 5 Hz SA. However, there is a cluster of data points for M4.0-5.0 earthquakes at distance of 700-1000 km that are lower than the predicted values for M4.5 (Figure 6.6). A more detailed comparison with the data needs to be done.

The variability of ground motions for different rupture parameters is illustrated in Figure 6.8. Here I show the 1Hz SA for M7.5 using different aspect ratios of the rupture, focal mechanisms, hypocenters, and slip distributions. At this frequency, the SA values are influenced by both the deterministic and stochastic parts of the broadband synthetics. Larger variability is observed at lower frequencies. The deterministic portion of the calculation produces more variability than the stochastic part, because it includes focal mechanism effects and stronger directivity effects.

For periods of 2 second and longer, the SA values from the simulations are affected by the depth of rupture. Figure 6.9 shows a case where the 3 second SA values are substantially decreased at distances of 40-200 km as the Dtor is increased from about 5 to 9 km, corresponding to hypocentral depths of 8 and 13 km, respectively. The more gradual decay with distance for the shallower source is probably caused by the larger surface waves for the shallower source. I found that increasing the Dtor from 1 to 5 km in the M7.5 and M8.0 simulations produced a significant decrease of SA values at periods of 2 second and longer. A key question is whether the intrinsic and scattering Q values for surface

waves are properly characterized in the crustal model used in the deterministic simulations.

The SA values for each magnitude were binned by distance and the median and standard deviation (in ln units) for each bin have been calculated and supplied to the NGA East TI Team. Figure 6.10 shows the binned values for 1 Hz SA for the M4.5, 5.5, 6.5, 7.5, and 8.0 simulations. The Moho reflection causes the increase of SA values at 100-200 km for the M4.5-6.5 results, which are controlled by the deterministic calculation at this frequency. For M7.5 and 8.0 there is a leveling off with distance of the SA values in this distance range caused partly by the stochastic part of the calculation. In addition, the finiteness of the source tends to blur out the SA peak from the Moho reflection in the deterministic synthetics. Figure 6.10 illustrates the saturation of 1 Hz SA with increasing magnitude at close-in distances.

The SA values were calculated at periods from 0.01-10 seconds. Figure 6.11 is a plot of the binned SA values at different periods from the M7.5 simulations, as a function of distance. At distances greater than about 200 km the SA values at higher frequencies tend to merge with those at lower frequencies, because of the effect of Q.

6.3 CONCLUSIONS

The PSA values derived in this study are based on a methodology that incorporates our knowledge of earthquake rupture histories and seismic-wave propagation. For low frequencies, the deterministic synthetics include phasing appropriate for earthquakes, including directivity effects and surface waves. The broadband synthetics essentially contain a frequency-dependent apparent geometrical spreading from 5-70 km distance, since the deterministic portion of the calculation includes radiation pattern and directivity that cause steeper decay than R^{-1} and the stochastic portion is based on R^{-1} spreading, consistent with observations. The SA values derived from these finite-fault simulations are appropriate for use in seismic hazard assessment in ENA.

6.4 ACKNOWLEDGMENTS

I thank David Boore and Stephen Hartzell for helpful reviews that led to improvements in this chapter.

References

Atkinson, G.M. and D.M. Boore (1995). Ground-motion relations for eastern North America, *Bull. Seism. Soc. Am*., **85**, 17-30.

Atkinson, G. M., and D.M. Boore (2006). Ground motion prediction equations for earthquakes in eastern North America. *Bull. Seism. Soc. Am.* **96**, 2181-2205.

Boore, D. M. (2005). SMSIM---Fortran Programs for Simulating Ground Motions from Earthquakes: Version 2.3---A Revision of OFR 96-80-A, U.S. Geological Survey Open-File Report, *U. S. Geological Survey Open-File Report* **00-509**, revised 15 August 2005, 55 pp.

Brune, J. N. (1970). Tectonic stress and the spectra of seismic shear waves from earthquakes, J. Geophys. Res. 76, 4997–5002.

Frankel, A. (1995). Simulating strong motions of large earthquakes using recordings of small earthquakes: the Loma Prieta mainshock as a test case, Bull. Seismol. Soc. Am. 85, 1144–1160.

Frankel, A.D. (2009). A constant stress-drop model for producing broadband synthetic seismograms—comparison with the Next Generation Attenuation relations: *Bull. Seism. Soc. Am*., **99**, p. 664–680.

Frankel, A. (2013). Rupture history of the 2011 M9 Tohoku Japan earthquake determined from strong-motion and high-rate GPS recordings: sub-events radiating energy in different frequency bands, *Bull. Seism. Soc. Am*., **103**, p. 1290-1306.

Frankel, A. (in press). Decay of S-wave amplitudes with distance for earthquakes in the Charlevoix, Quebec area: effects of radiation pattern and directivity, accepted for publication in *Bull. Seism. Soc. Am*.

Frankel, A., Mueller, C., Barnhard, T., Perkins, D., Leyendecker, E.V., Dickman, N., Hanson, S., and Hopper, M., (1996). National seismic hazard maps—Documentation June 1996, *U.S. Geological Survey Open-File Report 96-532*, 110 p.

Graves, R., and A. Pitarka (2004). Broadband time history simulation using a hybrid approach, in *13th World Conf. on Earthquake Engineering*, Vancouver, British Columbia, paper no. 1098.

Hartzell, S., C. Langer, and C. Mendoza (1994). Rupture histories of eastern North American earthquakes. *Bull. Seism. Soc. Am*., **84**, 1703-1724.

Hartzell, S., S. Harmsen, A. Frankel, and S. Larsen (1999). Calculation of broadband time histories of ground motion: comparison of methods and validation using strong ground motion from the 1994 Northridge earthquake, Bull. Seismol. Soc. Am. 89, 1484–1504.

Hartzell, S., A. Frankel, P. Liu, Y. Zeng and S. Rahman (2011). Model and parametric uncertainty in source-based kinematic models of earthquake ground motion, *Bull. Seism. Soc. Am.*, **101**, 2431-2452.

Leonard, M. (2010). Earthquake fault scaling; self-consistent relations of rupture length, width, average displacement and moment release, *Bull. Seismol. Soc. Am.*, **100**, 1971–1988.

Mai, P. M., and G. C. Beroza (2002). A spatial random field model to characterize complexity in earthquake slip, *J. Geophys. Res.*, **107**, 1–21.

Wells, D. L., and K. J. Coppersmith (1994). New empirical relationships among magnitude, rupture length, rupture width, and surface displacements, Bull. Seismol. Soc. Am. 84, 974–1002.

Zhu, L., and Rivera, L. (2002). Computation of dynamic and static displacement from a point source in multi-layered media, *Geophys. J. Int.*, **148**, 619–627.

Table 1. Velocity model used to make deterministic low-frequency synthetics (from Hartzell et al., 1994).

Vp (km/s)	Vs (km/s)	Density (g/cm^3)	Thickness (km)	Q_p	Q_s
4.5	2.6	2.3	1.44	500	250
5.5	3.4	2.5	6.	1000	500
6.1	3.5	2.67	12.	4000	2000
6.6	3.7	2.85	14.	4000	2000
7.0	4.0	3.02	10.	4000	2000
8.2	4.7	3.35		4000	2000

Table 2. Earthquake scenarios used in simulations to date. In some cases, multiple slip distributions and hypocenters were used for a given scenario.

Magnitude	Fault Dimensions (km)	Fault Mechanism	Dtor (km)	Approximate distance range (Rrup, km)
8.0	160 x 40	Strike slip, 90° dip	1	2-1000
8.0	160 x 40	Thrust, 45° dip	1	2-200
8.0	160 x 40	thrust	5	5-200
8.0	160 x 40	Strike slip	5	5-1000
7.5	80 x 25	Strike slip	1	2-1000
7.5	80 x 25	thrust	1	2-200
7.5	119 x 12	Strike slip	5	5-1000
7.5	80 x 25	Strike slip	5	5-1000
7.5	80 x 25	thrust	5	5-200
6.5	14 x 10	Strike slip	5	5-1000
6.5	14 x 10	thrust	5	5-200
5.5	3.9 x 3.9	Strike slip	5	5-1000
5.5	3.9 x 3.9	thrust	5	5-200
5.5	3.9 x 3.9	Strike slip	9	9-200
4.5	1.2 x 1.2	Strike slip	5	5-1000
4.5	1.2 x 1.2	thrust	5	5-200
4.5	1.2 x 1.2	Strike slip	12	12-200

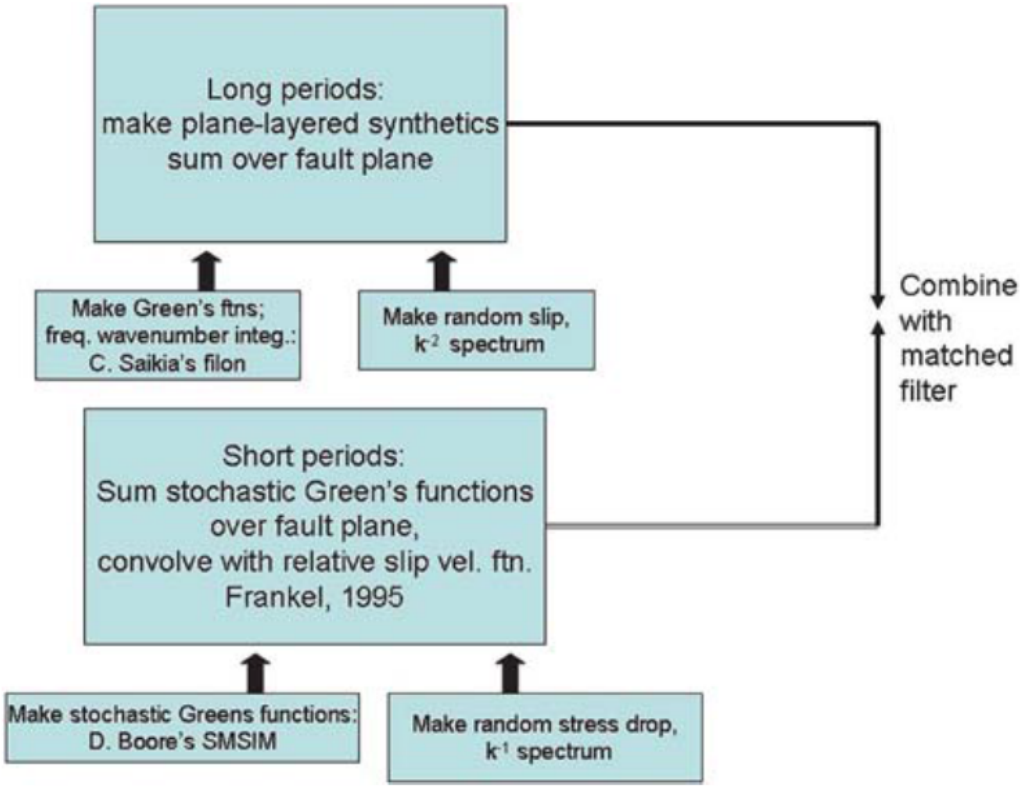

Fig 6.1. Flow chart of procedure to make hybrid broadband synthetics, from Frankel (2009). The frequency-wavenumber integration code used in the ENA simulations was from Zhu and Rivera (2002).

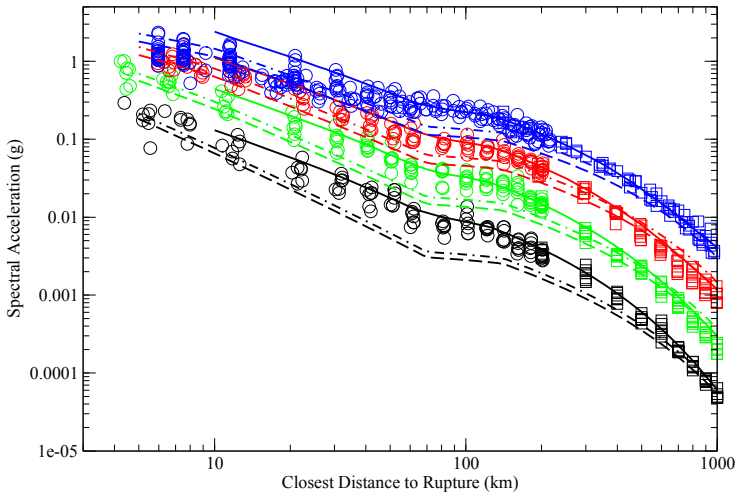

Figure 6.2. 5 Hz SA for M4.5 (black circles), M5.5 (green circles), M6.5 (red circles), and M7.5 (blue circles) from the simulations. The plotted values are a representative sub-set of all the simulation results for that magnitude. Solid lines are predicted values from Frankel et al. (1996). Dashed lines are predicted values from Atkinson and Boore (2006). Dot dash lines are predicted values from Atkinson and Boore (2006) using stress drop of 200 bars. Lines with predicted values are color coded by magnitude.

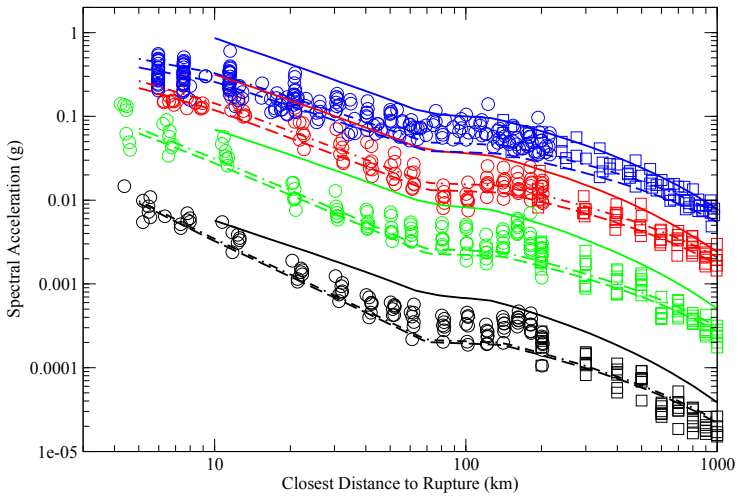

Figure 6.3. 1 Hz SA for M4.5 (black circles), M5.5 (green circles), M6.5 (red circles), and M7.5 (blue circles) from the simulations. The plotted values are a representative sub-set of all the simulation results for that magnitude. Solid lines are predicted values from Frankel et al. (1996). Dashed lines are predicted values from Atkinson and Boore (2006). Dot dash lines are predicted

values from Atkinson and Boore (2006) using stress drop of 200 bars. Lines with predicted values are color coded by magnitude.

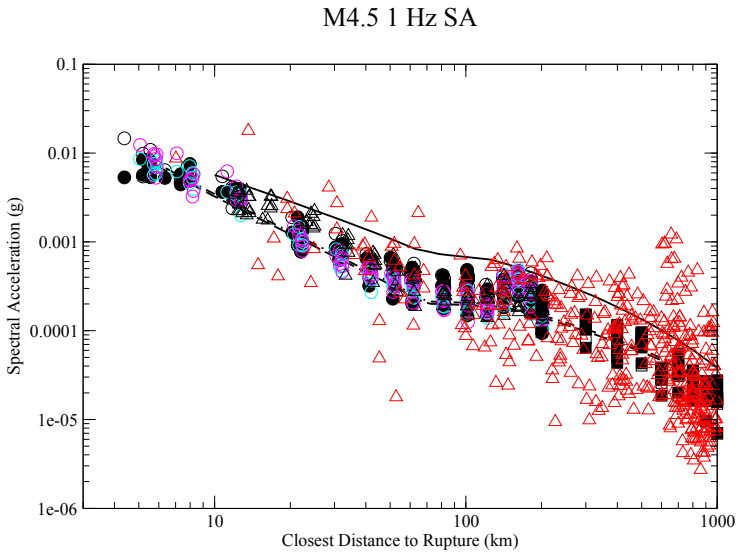

Fig 6.4. 1 Hz SA from M4.5 simulations (filled and open black circles and filled squares) plotted with observed values from NGA East database (red triangles). Only observed values for sites with Vs30 greater than 760 m/s were plotted. The observed values were not adjusted for Vs30. Solid lines are predicted values from Frankel et al. (1996). Dashed lines are predicted values from Atkinson and Boore (2006). Dot dash lines are predicted values from Atkinson and Boore (2006) using stress drop of 200 bars.

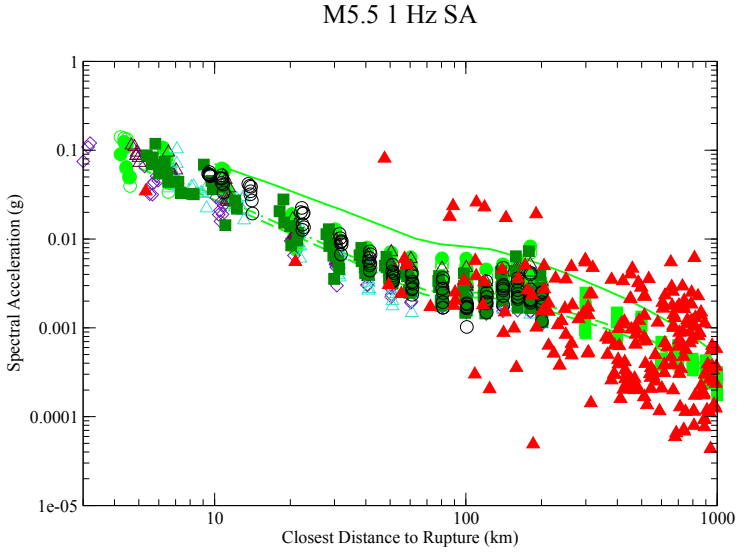

Fig. 6.5. 1 Hz SA from M5.5 simulations (filled and open green circles and filled squares) plotted with observed values from NGA East database (red triangles). Only observed values for sites with Vs30 greater than 760 m/s were plotted. The observed values were not adjusted for Vs30. Lines represent predictions from Frankel et al. (1996) and Atkinson and Boore (2006); see caption for figure 6.2.

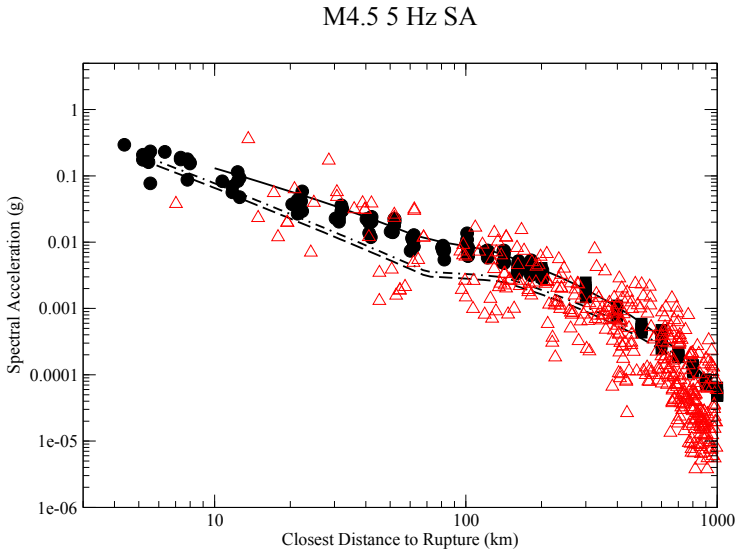

Fig 6.6. 5 Hz SA from M4.5 simulations (filled black circles and filled squares) plotted with observed values from NGA East database (red triangles). Only observed values for sites with Vs30 greater than 760 m/s were plotted. The observed values were not adjusted for Vs30. Solid lines are predicted values from Frankel et al. (1996). Dashed lines are predicted values from Atkinson and Boore (2006). Dot dash lines are predicted values from Atkinson and Boore (2006) using stress drop of 200 bars.

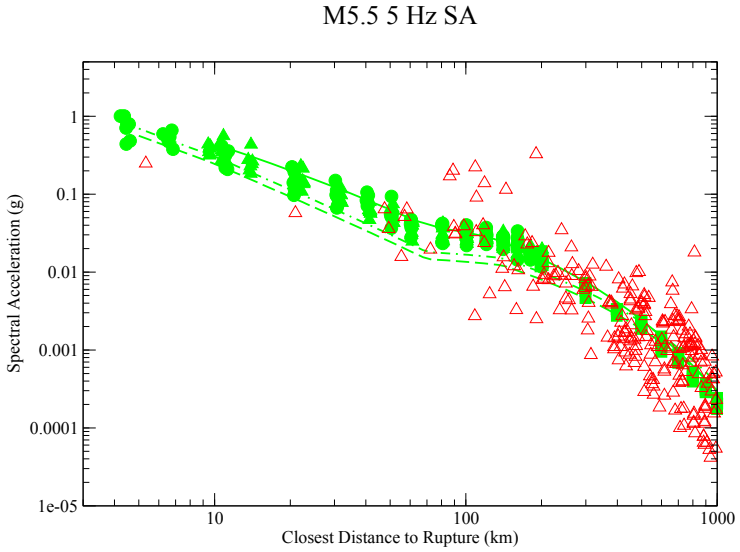

Fig 6.7. 5 Hz SA from M5.5 simulations (filled and open black circles and filled squares) plotted with observed values from NGA East database (red triangles). Only observed values for sites with Vs30 greater than 760 m/s were plotted. The observed values were not adjusted for Vs30. Solid lines are predicted values from Frankel et al. (1996). Dashed lines are predicted values from Atkinson and Boore (2006). Dot dash lines are predicted values from Atkinson and Boore (2006) using stress drop of 200 bars.

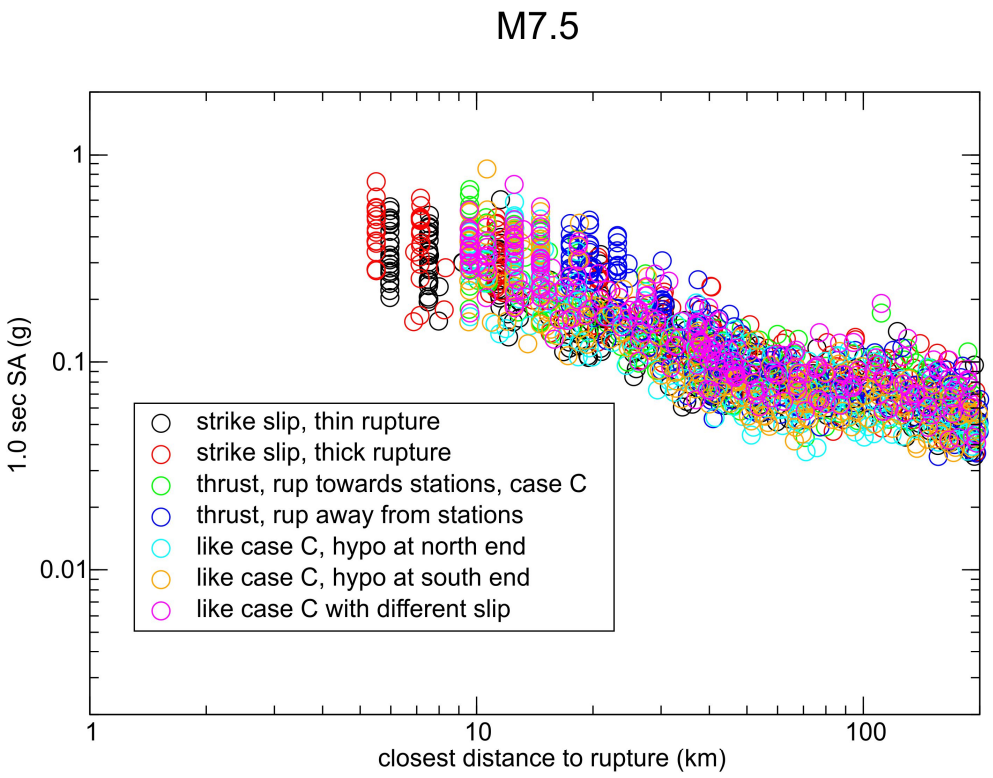

Fig 6.8. 1.0 second SA values for the various M7.5 simulations with different rupture characteristics.

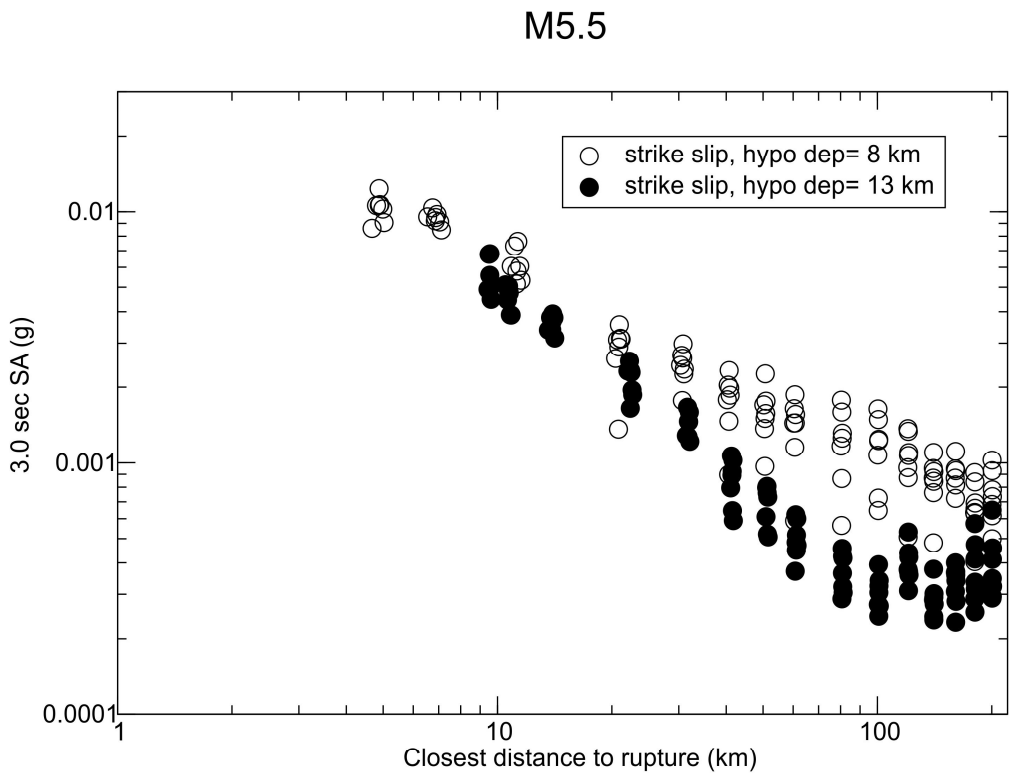

Fig 6.9. 3.0 second SA values from two of the M5.5 simulations showing the effect of changing the depth of the rupture.

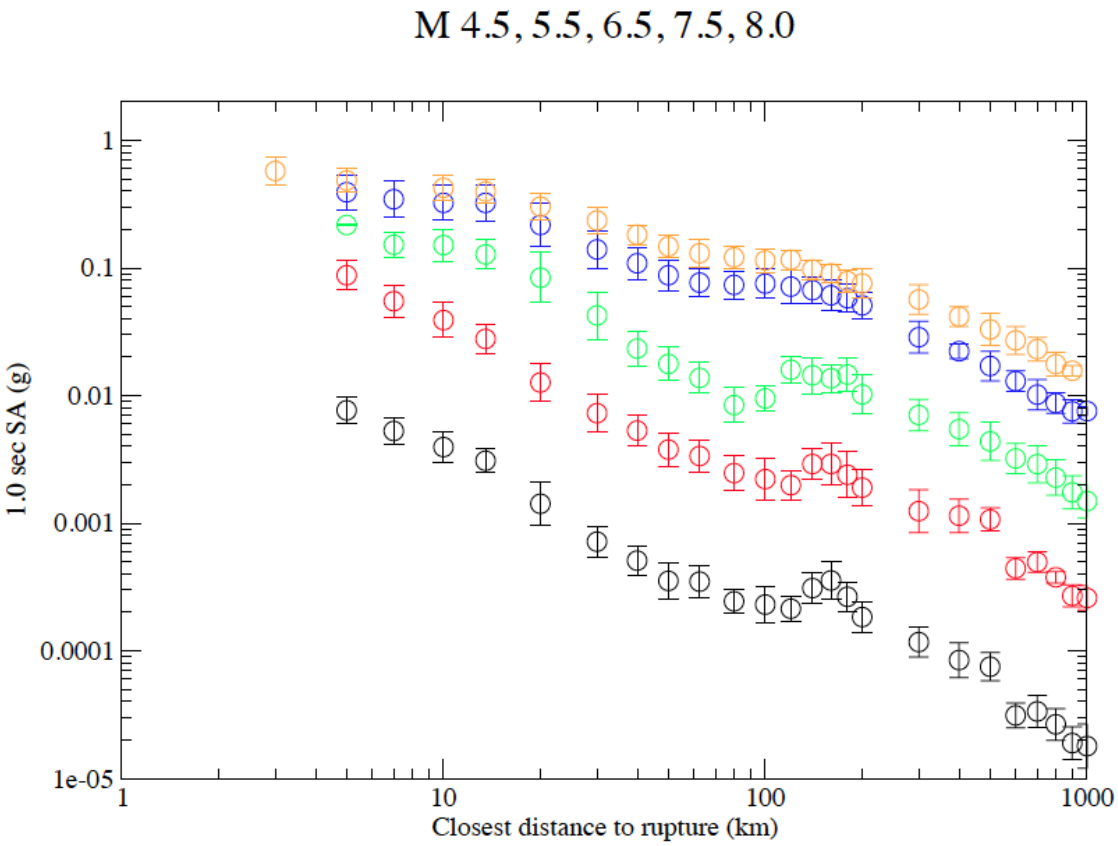

Fig 6.10. 1.0 second SA values binned by distance, for all of the magnitudes studied. Dtor ≥ 5 km.

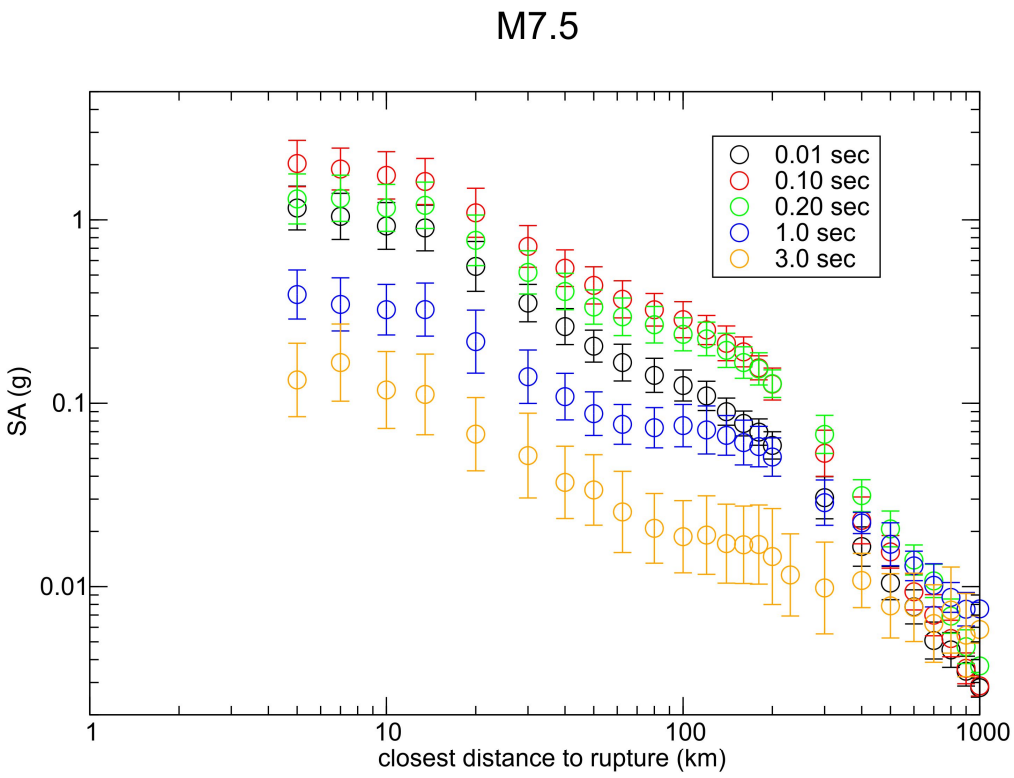

Fig 6.11. SA values for various periods for the M7.5 simulations, binned by distance.